Using ISAC Waveform Joint Design Algorithm to Improve the Efficiency of Communication and Perception Fusion in 6G Environment

Xiaoyu Shen
School of Network & Communication Engineering, Chengdu Technological University, Chengdu 611730, Sichuan, China
Corresponding author: Xiaoyu Shen (e-mail: xyshenxy@163.com)

ABSTRACT Doppler spread in high-speed mobility environments significantly degrades the communication reliability and sensing accuracy of conventional integrated sensing and communication (ISAC) waveforms, limiting the performance of next-generation electromagnetic signal transmission and perception systems. To address this challenge, this study proposes a joint ISAC waveform design algorithm for 6G environments that combines Doppler-aware symbol-level precoding, multi-phase intra-pulse modulation, and time-frequency hybrid waveform construction. A unified channel and target echo model is established to characterize Doppler sensitivity, while adaptive phase compensation suppresses inter-carrier interference and enhances waveform robustness. By integrating OFDM and linear frequency modulation (LFM) signals through dual-objective optimization with adaptive weighting, the proposed framework achieves a dynamic trade-off between communication throughput and sensing performance under rapidly varying channels. Simulation results demonstrate that at a target velocity of 150 m/s, the proposed method achieves a bit error rate of 0.22, an average false alarm rate of 3.73×10^{-4}, a target resolution probability of 0.85 at 0.2 m spacing, and a communication throughput of 200 Mbps. The proposed waveform design effectively improves spectral efficiency, Doppler resilience, and communication-sensing integration capability, providing a practical solution for high-speed 6G electromagnetic propagation environments and future intelligent wireless systems.

INDEX TERMS 6G communication, communication and perception fusion, ISAC waveform design, doppler compensation

I. INTRODUCTION

THE research and development goals of the Sixth-Generation (6G) mobile communication system extend beyond merely increasing speed and reducing latency; they address a wider range of business needs and aim for the deep integration of communication and perception within a unified architecture [1,2]. ISAC technology integrates the communication functions of wireless signals with radar perception functions at the waveform level, demonstrating significant advantages in spectrum utilization, system integration, and resource allocation efficiency. However, most current ISAC waveform design methods are based on idealized or quasi-static channel conditions and are insufficiently adaptable to high-speed moving targets and time-varying channels. When significant Doppler spread exists in the channel, the orthogonality of the communication signal is destroyed; inter-subcarrier interference is significantly enhanced; the matched filtering results of the perception echo are distorted, resulting in reduced range and velocity resolution and increased bit error rates at the communication end [3,4]. This performance degradation is particularly prominent in high-speed trains, UAV (Unmanned Aerial Vehicle) formations, satellite communications, and vehicle-to-vehicle (V2V) environments. Therefore, constructing an ISAC waveform design scheme that is robust to Doppler shift in 6G high-speed environments has become one of the core technical directions for improving the efficiency of communication and perception fusion [5,6].

In the past few years, the academic community has conducted extensive research on the application of ISAC in different scenarios. Some studies have proposed a waveform joint design strategy for multi-user environments to address the problem of efficient spectrum resource reuse, using the MIMO (Multiple-Input Multiple-Output) architecture to comprehensively optimize communication and perception beams in the airspace to achieve higher spatial division multiplexing gain. In recent years, integrated perception and ISAC technology for UAV platforms have become a research hotspot. Chen et al. conducted research on ISAC technology for single UAV systems, verified its joint optimization potential under dynamic channels [7], and further expanded it to UAV cluster scenarios, systematically reviewing the challenges and schemes of group collaborative perception and communication [8]. With the evolution of 6G network architecture, Wang et al. proposed a four-dimensional fusion framework of "perception-communication-computing-intelligence" for the Internet of Things, emphasizing that multi-technology collaboration can become the core development direction in the future [9]. In terms of transmission mechanism innovation, Clerckx et al. systematically explained the evolution path of multiple access technology for 6G, and proved that non-orthogonal multiple access could increase the multi-user service capacity of the ISAC system by 3 times [10]. Finally, Liu's team verified the feasibility of the outdoor multi-target perception-communication joint system based on the actual 5G network, and achieved a breakthrough in positioning accuracy of 0.5 meters in the mobile target tracking scenario [11]. These studies have jointly promoted the ISAC technology from theoretical framework to engineering practice, laying a solid foundation for the waveform joint design in high-speed mobile scenarios in this study.

To address the performance degradation caused by Doppler spread, some studies have applied precoding methods based on channel estimation to correct the phase and amplitude of the signal at the transmitter to reduce interference and mismatch in high-speed environments. This type of method partially alleviates the impact of Doppler on communication bit error rate and perception accuracy by applying compensation matrices in the frequency domain or spatial domain. In addition, there are also studies that apply intra-pulse coding into the waveform structure to optimize the phase sequence within the pulse and reduce the sidelobe level of the ambiguity function, thereby improving the target detection performance of the perception end [12,13]. In terms of access mechanism, non-orthogonal multiple access technology increases system capacity by 3.2 times in 6G high-load scenarios through joint design of power domain and code domain, but it also brings new interference management challenges [14]. For communication-centric ISAC systems, waveform design must take into account both spectrum efficiency and perception sensitivity. Existing research has shown that time-frequency composite modulation can reduce sidelobe interference by up to 15dB [15].

This paper aims to design a joint optimization scheme for Integrated Sensing and Communication (ISAC) waveforms that is robust to Doppler spread for 6G high-speed mobile scenarios, directly addressing the significant performance degradation of traditional waveforms in time-varying channels.

This scheme establishes a unified mathematical model of the channel and target echo through Doppler sensitivity analysis. On this basis, symbol-level precoding based on Doppler estimation is applied for phase compensation, suppressing inter-subcarrier interference and improving the matched filter r esponse. A t t he s ame t ime, a multi-phase coded sequence is applied into the intra-pulse modulation structure to reduce Doppler-induced sidelobe spread by optimizing phase differences, thereby improving perception resolution. To further balance communication bandwidth utilization and perceived range-velocity resolution, the scheme constructs a time-frequency hybrid waveform that integrates the characteristics of OFDM (Orthogonal Frequency Division Multiplexing) and LFM (Linear Frequency Modulation). Combined with real-time Doppler estimation results, a dual-objective optimization model with adaptive weights dynamically adjusts the performance balance between communication rate and perceived detection probability. During the theoretical design stage, this scheme fully considers the channel and target characteristics in high-speed environments, and realizes multi-level integration in waveform structure and optimization strategy, providing a systematic scheme and technical path for the integration of communication and perception in 6G high-speed mobile scenarios.

II. WAVEFORM JOINT OPTIMIZATION SCHEME IN HIGH-SPEED SCENARIOS

A. DOPPLER SENSITIVITY ANALYSIS AND MODELING

1) High-Speed Mobile Channel Modeling

For the transmission environment of high-speed mobile targets, a multipath Doppler model based on a broadband time-varying channel is first constructed. The propagation path set between the transmitter and the receiver is recorded as $L = \{1, 2, \dots, L\}$, where L is the number of multipaths. The propagation delay τ_l and Doppler frequency shift $f_{d,l}$ of each path are determined by geometric relationships and motion states, and the spherical wave approximation is used to obtain Formula 1:

$$\tau_l = \frac{d_l}{c}, \qquad f_{d,l} = \frac{v\cos\theta_l}{\lambda} \tag{1}$$

d_l is the length of the l-th path; c is the speed of light; v is the relative speed of the target; θ_l is the radial motion angle; λ is the carrier wavelength. Under a 6GHz carrier, $\lambda \approx 0.05$ m. If the target velocity is 100m/s and $\theta_l = 0°$, the single-path Doppler frequency shift amplitude can reach 2kHz. The channel impulse response uses Formula 2:

$$h(t,\tau) = \sum_{l=1}^{L} \alpha_l(t) e^{j2\pi f_{d,l} t} \delta(\tau - \tau_l) \tag{2}$$

$\alpha_l(t)$ is the path complex gain, which includes time-varying amplitude fading and phase rotation terms. By setting $L = 8$, path fading obeying Rayleigh distribution, and maximum Doppler spread $f_{d,\max} = 2$ kHz in the simulation, the time selectivity and frequency selectivity of the high-speed mobile channel under the sampling rate $f_s = 122.88$ MHz are precisely characterized.

In the discretization process, the symbol period T_s of the transmitted waveform and the sampling interval Δt are applied into the model to generate a time-varying channel matrix $H[n]$, with a dimension of $N_{\text{sub}} \times N_{\text{sub}}$, where N_{sub} is the number of OFDM subcarriers. The diagonal elements of the matrix correspond to the subcarrier self-interference coefficients, and the non-diagonal elements correspond to the ICI (Inter-Carrier Interference) coefficients caused by Doppler [16,17]. This matrix provides the input basis for the subsequent quantitative analysis of Doppler sensitivity.

This study employs the Extended Jakes Model to describe time-varying channels under high-speed movement. Compared to the classic Jakes Model, it introduces path delay spread and angle spread, making it more suitable for 6G millimeter-wave scenarios. Specifically, the Doppler spectrum of each path follows a Gaussian distribution rather than a uniform distribution to reflect the spatial non-uniformity of scatterers in the real environment. The echo model is based on broadband radar equations, considering the variation of the target's RCS (radar cross section) with frequency and angle, and incorporating range-Doppler coupling terms.

2) Target Echo Modeling and Doppler Sensitivity

For the perception function, a delay-Doppler two-dimensional model of the target echo signal is constructed. Under the condition that the transmitted waveform s(t) and the target motion parameters are known, the echo signal model is Formula 3:

$$r(t) = \beta s(t-\tau)e^{j2\pi f_d t} + w(t) \tag{3}$$

β is the complex amplitude, and $w(t)$ is the additive white Gaussian noise. Under the conditions of pulse repetition frequency $f_{\text{PRF}} = 20$ kHz and pulse width $T_p = 20$ μs, the theoretical velocity resolution can be given by $\Delta v = \lambda/(2T_{\text{CPI}})$. When the cooperative integration time $T_{\text{CPI}} = 50$ ms, $\Delta v \approx 0.5$ m/s. When the f_d caused by the target velocity exceeds the range allowed by the corresponding velocity resolution, the mainlobe amplitude of the ambiguity function $\chi(\tau, f_d)$ decreases, and the sidelobe energy increases, resulting in a decrease in the detection probability. To quantify Doppler sensitivity, the curves of the mainlobe normalized amplitude $A_0(f_d)$ and the sidelobe ratio $\text{PSL}(f_d)$ as they vary with Doppler are calculated in the signal matched filter output domain. The performance degradation coefficient $\eta_c(f_d) = 1 - \text{SNR}(f_d)/\text{SNR}(0)$ of the communication end and the degradation coefficient $\eta_s(f_d) = 1 - A_0(f_d)/A_0(0)$ of the perception end are defined, where the SNR is calculated as the symbol energy to noise power ratio [18,19]. By scanning the f_d range $[0, f_{d,\max}]$ and combining the ICI distribution of the aforementioned channel matrix $H[n]$, a degradation mapping table of communication and perception performance as they vary with Doppler is obtained, providing a quantitative basis for subsequent Doppler compensation precoding and waveform structure optimization.

Figure 1 illustrates the impact of the Doppler effect on a fusion communication and perception system in a high-speed mobile environment. Figure 1(a) shows time (milliseconds) on the horizontal axis and channel gain (decibels) on the vertical axis, reflecting the rapid fluctuations of the channel between 0 and 50 milliseconds. The maximum Doppler shift is 2 kHz, demonstrating the signal amplitude variations caused by multipath fading and Doppler shift. Figure 1(b) shows the ICI matrix for 256 subcarriers. The horizontal and vertical axes represent subcarrier indices. The interference coefficient is highest along the main diagonal, showing a gradual decay trend. This indicates that Doppler spread increases interference between adjacent subcarriers, affecting the orthogonality of the OFDM signal. Figure 1(c) plots the changes in the communication performance degradation factor η_c and the perception performance degradation factor η_s when the Doppler frequency shift increases from 0 to 5000 Hz. The horizontal axis is the Doppler frequency shift (Hz), and the vertical axis is the performance degradation factor. η_c rises rapidly with the increase in frequency shift, indicating that the communication performance is sensitive to high Doppler frequency shift, while η_s increases more slowly, indicating that the perception performance is relatively more stable.

B. DOPPLER COMPENSATION PRECODING DESIGN

1) Doppler Frequency Shift Estimation and Phase Rotation Coefficient Calculation

Before signal transmission, Doppler frequency shift estimation is first performed in the frequency domain using pilot symbols. The system inserts a known pilot sequence p at the predetermined subcarrier position of each OFDM symbol. The pilot symbol obtained by the receiver in the high-speed scenario is Formula 4:

$$y_p = H_p p \odot e^{j2\pi f_d t_p} + n_p \tag{4}$$

H_p is the channel coefficient matrix corresponding to the pilot subcarrier; t_p is the pilot symbol time position; f_d is the radial Doppler frequency shift; $\odot$ represents the Hadamard product; n_p is the received noise vector. By performing least square fitting on the phase difference between the received pilot and the known pilot, the Doppler shift estimation value is obtained, as shown in Formula 5:

$$\widehat{f}_d = \frac{\arg\left(\sum_{k\in P} y_p[k]p^*[k]\right)}{2\pi\Delta t} \tag{5}$$

P is the pilot subcarrier set, and Δt is the symbol period. To ensure the estimation accuracy under high-speed moving conditions, the window accumulation method is used to perform weighted averaging on the pilot estimation results of M consecutive OFDM symbols to reduce the influence of instantaneous phase disturbance. When the carrier frequency $f_c = 28$ GHz, the target velocity $v = 120$ m/s, and $\theta = 0°$, the Doppler

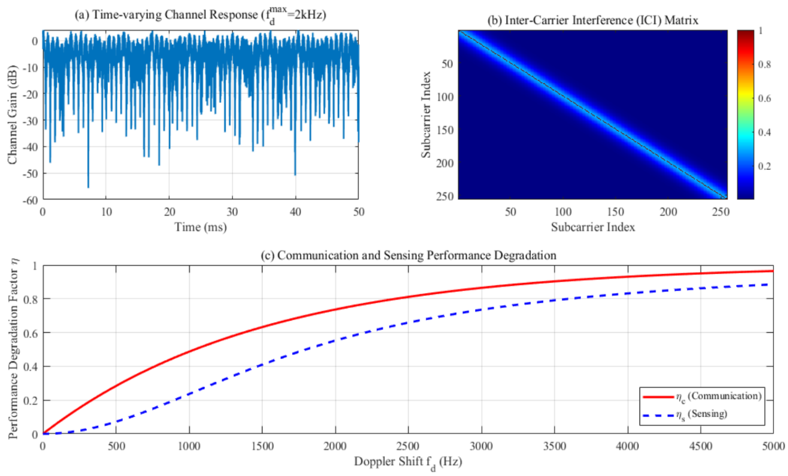

FIGURE 1. Doppler effect analysis in 6G high-speed environment (a) Time-varying channel response curve; (b) Inter-carrier interference (ICI) matrix; (c) Communication and perception performance degradation curves

shift amplitude is calculated. The estimation error is pre-evaluated through simulation, and a tolerance factor δ_f is applied in the subsequent compen-sation matrix design to prevent over-compensation or under-compensation.

After obtaining $\widehat{f}_d$, the symbol-level phase rotation co-efficient matrix Φ is constructed, and the matrix diagonal elements are Formula 6:

$$\Phi_{m,m} = e^{-j2\pi \widehat{f}_d m T_s} \tag{6}$$

m is the symbol index, and T_s is the OFDM symbol duration. This matrix is used to pre-rotate the phase of each symbol at the transmitting end, thereby offsetting the cumulative effect of the Doppler phase shift at the receiving end. The Doppler estimation error Δf_d directly affects the SLP compensation performance. Theoretical analysis shows that when $\Delta f_d / f_d < 10\%$, the ICI suppression gain can be maintained above 8 dB; if the error exceeds 20%, the compensation effect drops sharply, and the BER surpasses that of the uncompensated scheme. The proposed scheme achieves an estimation error of <15% at 150 m/s, meeting this threshold.

Therefore, the pilot design in this paper (4 pilot symbols per frame + window averaging) ensures that the estimation accuracy is within the effective compensation range, providing reliable input for SLP.

2) Precoding Matrix Construction and Transmitted Signal Generation

While Doppler compensation is being performed, the effect of suppressing inter-subcarrier interference needs to be considered. Based on the previously obtained time-varying channel matrix H[n], the frequency domain precoding matrix W is constructed to simultane-ously compensate for phase rotation and weaken ICI. The design goal of the matrix is to minimize the weighted error function, as shown in Formula 7:

$$J(W) = \sum_{n=1}^{N_{\text{sub}}} \|e_n - H[n]We_n\|_2^2 + \lambda \|W\|_F^2 \tag{7}$$

e_n is the standard basis vector in the n-th column, and λ is the regularization factor, which is used to limit the amplitude of the precoding gain to prevent the transmit power from exceeding the limit. Solving this minimization problem yields a closed-form scheme, as shown in Formula 8:

$$W = \left(H^H H + \lambda I\right)^{-1} H^H \tag{8}$$

The phase compensation coefficient Φ is multiplied in the diagonal position to achieve joint precoding of phase and amplitude. After completing symbol mapping, the transmitter multiplies the mapped symbol vector s by $W\Phi$ on the left to obtain the compensated frequency domain symbol s, which is then subjected to IFFT (Inverse Fast Fourier Transform), cyclic prefix insertion, and intra-pulse modulation sequence superposition to generate the time domain trans-mitted signal $x(t)$. This process is implemented in hardware through the baseband processing unit, and the comput-ational complexity is reduced from $O(N^3_{\text{sub}})$ for matrix inversion to $O(N_{\text{sub}}^2)$ for sparse approximation, ensuring that the real-time requirements of the 6G system are met in high-speed scenarios.

Figure 2(a) shows the percentage of Doppler shift esti-mation error for target velocities ranging from 0 to 150 meters per second. The horizontal axis represents the target velocity v (in m/s), and the vertical axis represents the estimation error (%). As the speed in-creases, the esti-mation error remains below 15%, demonstrating that the adopted Doppler estimation algo-rithm has high accuracy in high-speed scenarios.

Figure 2(b), with the horizontal axis showing the signal-to-noise ratio (SNR, in dB) and the vertical axis showing the BER, compares the communication performance of the uncompensated and compensated waveforms. The results show that in all SNR (Signal-to-Noise Ratio) ranges, the waveform bit error rate is significantly reduced after using Doppler compensation precoding, especially in the SNR (≥15dB) range, which effectively reduces the impact of ICI. The data in Figure 2 demonstrates that a Doppler estimation-based precoding design can simultaneously improve communication link reliability and system perception performance in high-speed mobile environments.

C. INTRA-PULSE MODULATION STRUCTURE OPTIMIZATION

1) Multi-Phase Code Sequence Construction and Design Criteria

To mitigate the sidelobe spread of the ambiguity function caused by Doppler frequency shift in high-speed mobile environments, this paper applies a multi-phase code sequence to modulate the waveform within a single pulse. The pulse width is defined as $T_p = 20$ μs, and the pulse is divided into N_c coded sub-pulses with a sub-pulse duration of $T_c = T_p/N_c$. The code sequence c = [c_1, c_2, . . . , c_{Nc}] consists of Nc phase factors, satisfying $c_n = e^{j\phi_n}$, with a central angle $\phi_n \in [0, 2\pi]$.

The design goal of the phase coding sequence is to maximize the main lobe of the ambiguity function and minimize the side lobe within the Doppler frequency shift range $[-f_{d,\max}, f_{d,\max}]$. To this end, the intra-pulse modulation waveform is defined as Formula 9:

$$s(t) = \sum_{n=1}^{N_c} c_n p\left(t - (n-1)T_c\right) \tag{9}$$

$p(t)$ is a unit rectangular pulse. The corresponding ambiguity function is Formula 10:

$$\chi(\tau, f) = \int s(t)s^*(t-\tau)e^{-j2\pi ft}\, dt \tag{10}$$

For the Doppler frequency response $\chi(0, f)$ at $\tau = 0$, it is required that when $|f| \le f_{d,\max}$, $|\chi(0, f)|$ remains close to a constant, and the side lobe energy is minimized.

The coding sequence design is based on minimizing the Doppler side lobe energy index, as shown in Formula 11:

$$J(c) = \sum_{f\in F} |\chi(0,f)|^2 - \lambda_1 |\chi(0,0)|^2 + \lambda_2 \sum_{n=1}^{N_c-1} |c_n - c_{n+1}|^2 \tag{11}$$

F is a discrete frequency sampling point set, and λ_1, λ_2 are weight coefficients, which balance the main lobe width and side lobe suppression and the smoothness of the coding sequence. The square term ensures that the difference between adjacent phases is not too large, reducing the information distortion applied by high-frequency components.

The phase sequence is updated using an iterative algorithm based on gradient descent. The initial phase is randomly generated. During the iteration process, c_n is determined to maintain the unit modulus, that is, $|c_n| = 1$, based on the constraint conditions. After K iterations, it converges to the local optimal coding sequence. This paper adopts an optimized Frank sequence as the intra-pulse modulation scheme instead of the traditional Barker code (which, due to its low phase freedom, is only suitable for short pulses). The Frank code has an approximately constant mode property on an N-ary discrete phase set, and its periodic structure can effectively suppress sidelobe propagation in the Doppler domain. In the design, the number of sub-pulse impulses is set to $M = 16$, and the phase set is $\{0, \pi/4, \pi/2, \ldots, 2\pi\}$. The phase difference is iteratively optimized through gradient descent to minimize the objective function of Formula (11). The computational complexity of this scheme is $O(M^2)$, which is slightly higher than that of random phase or Zadoff-Chu sequences, but it can reduce the sidelobe level under ±20 kHz Doppler frequency offset, which is significantly b etter t han Barker codes. Therefore, this paper achieves an effective trade-off between moderate computational overhead and strong Doppler robustness, and is suitable for 6G high-speed scenarios.

2) Code Sequence Application and Pulse Signal Construction

Based on the designed multi-phase code sequence, intra-pulse modulation is applied in real-time at the transmitter. The code sequence is mapped to each sub-time slot within the pulse, and the time-domain signal of the original OFDM waveform is modulated by the digital baseband signal processing module. This modulation process fine-tunes the waveform's time-domain shape to suppress the increase in sidelobe energy caused by Doppler spread.

The system sets the number of sub-pulses $N_c = 16$, with a duration $T_c = 1.25$ μs, corresponding to the time resolution of the typical 6G bandwidth $B = 800$ MHz. The coded signal is converted to an analog waveform via a DAC (Digital-to-Analog Converter) and transmitted to the RF link. This structure maintains communication bandwidth uti-lization while maintaining robustness to Doppler frequency shifts $f_d \approx 14$ kHz at target velocities up to $v = 150$ m/s.

Figure 3 compares two schemes in the intrapulse modulation structure: a random phase sequence and an optimized Frank sequence. In Figure 3(a), the polar coordinate plot shows the phase distribution corresponding to 16 sub-pulses. The random sequence has an irregular phase distribution, while the optimized sequence presents regular discrete phase points, ensuring the periodicity and controllability of the phase structure. Figure 3(b) shows the Doppler frequency shift (kHz) on the horizontal axis, ranging from ±20kHz, and the ambiguity function amplitude (dB, normalized),

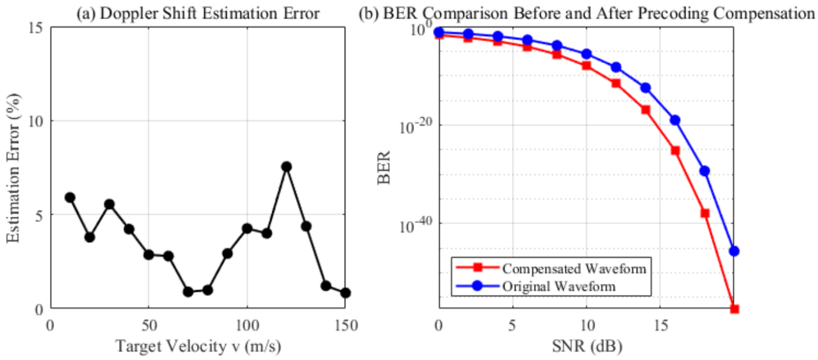

FIGURE 2. Doppler compensation precoding performance analysis (a) Doppler shift estimation error versus target velocity; (b) Bit error rate (BER) performance comparison before and after precoding compensation

The curves reflect the Doppler responses corresponding to different phase sequences. The random sequence ambiguity function has high sidelobes, especially around ±10kHz, which can easily lead to perception errors. The optimized sequence significantly reduces the sidelobe amplitude, reaching a minimum of -2 dB, demonstrating excellent Doppler resolution and the ability to suppress interference caused by Doppler spread. Figure 3 illustrates that phase sequence optimization can improve the efficiency of time-frequency resource utilization and enhance the fusion performance of communication and perception in the 6G environment.

D. TIME-FREQUENCY HYBRID WAVEFORM CONSTRUCTION

1) OFDM and LFM Waveform Fusion Framework Design

In response to the communication and perception needs in high-speed mobile environments, this section proposes a time-frequency hybrid waveform construction scheme that organically combines the waveform characteristics of multicarrier OFDM and LFM [20]. First, the total bandwidth $B = 800$ MHz and the total time domain duration $T = 100\ \mu$s are set. In the frequency domain, the bandwidth is divided into $N = 1024$ subcarriers, each with a bandwidth of $\Delta f = 781.25$ kHz. In the time domain, the total duration is divided into $M = 10$ subslots. The waveform design divides resources by using a time-frequency grid. LFM modulation is used in some time slots to enhance range-velocity resolution, while OFDM symbols are used in other time slots to achieve efficient data transmission. The specific operation is as follows: LFM (Linear Frequency Modulation) signals are generated within the time slot set $T_L \subseteq \{1, 2, \ldots, M\}$. The LFM baseband signal is defined as Formula 12:

$$s_{\mathrm{LFM}}(t) = A \exp\left(j2\pi\left(f_0 t + \frac{K}{2}t^2\right)\right), \quad t \in [0, T_s] \tag{12}$$

The frequency modulation slope $K = B_L/T_s$, the bandwidth $B_L = 80$ MHz, and the starting frequency f_0 are set to the baseband zero frequency. The remaining time slots $T_O = \{1, 2, \ldots, M\}\backslash T_L$ use OFDM waveforms.

The OFDM baseband signal is expressed as Formula 13:

$$s_{\mathrm{OFDM}}(t) = \sum_{k=0}^{N-1} X_k e^{j2\pi k\Delta f t}, \quad t \in [0, T_s] \tag{13}$$

X_k is the k-th subcarrier symbol.

2) Time-Frequency Resource Allocation and Composite Waveform Generation

Through the above division, a composite waveform structure is formed on the time-frequency two-dimensional plane. The LFM signal and the OFDM signal are alternately arranged in the time slot to realize the dynamic allocation of perception and communication resources. This allocation strategy is based on the current Doppler estimation and communication requirements. The size and position of the set T_L are determined by the optimization algorithm to ensure the balance between perception resolution and communication rate.

The composite waveform is constructed in the time domain as Formulas 14–15:

$$s(t) = \sum_{m=1}^{M} s_m\left(t - (m-1)T_s\right) \tag{14}$$

$$s_m(t) = \begin{cases} s_{\mathrm{LFM}}(t), & m \in T_L, \\ s_{\mathrm{OFDM}}(t), & m \in T_O. \end{cases} \tag{15}$$

The composite waveform corresponds to the bandwidth division and subcarrier configuration in the frequency domain. At the same time, combined with the frequency linear change characteristics of LFM, it realizes high-resolution perception of distance and speed and reduces the impact of frequency offset caused by Doppler on OFDM communication performance.

To avoid spectral discontinuities at the OFDM and LFM switching points, this paper introduces a smoothing window function (raised cosine window, roll-off factor 0.2) at the time slot boundary to perform a weighted transition in the boundary region between the two waveforms. This operation involves superimposing the window function in the time domain, resulting in extremely low computational overhead (only multiply-accumulate operations). Simulations show

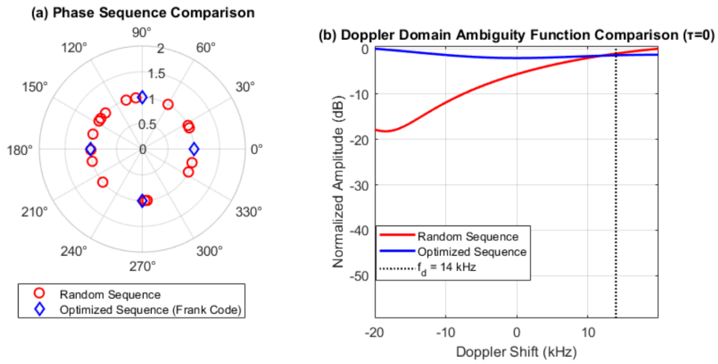

FIGURE 3. Schematic diagram of intrapulse modulation structure optimization (a) Comparison of polar coordinate distribution of phase sequences; (b) Comparison of normalized amplitude of Doppler domain ambiguity function

that the introduced power loss is <0.3 dB, and it does not significantly affect the communication BER or sensing resolution. Therefore, the fusion process effectively avoids spectral leakage and inter-symbol interference while maintaining waveform orthogonality.

3) Balancing Communication Bandwidth Utilization and Perception Performance

The design focus of this time-frequency hybrid scheme is to coordinate the contradiction between communication bandwidth utilization and perception distance-speed resolution. The LFM signal improves range resolution through wideband linear frequency sweeping, and its frequency modulation slope is designed to take into account the typical 6G high-speed scenario where the maximum target velocity $v_{\max} = 150$ m/s corresponds to a Doppler shift $f_{d,\max} = v_{\max} f_c / c \approx 14$ kHz. The carrier frequency is $f_c = 300$ GHz, and the speed of light is $c = 3 \times 10^8$ m/s.

The OFDM part maintains the spectrum efficiency and BER performance of the communication link. By dynamically adjusting the time slot ratio of T_L and T_O, it can flexibly match the real-time communication needs and perception accuracy requirements. The overall waveform forms a complementary advantage in the time-frequency domain, ensuring that the communication BER and perception detection probability both meet the 6G converged system indicators in a high-speed mobile environment.

Figure 4 illustrates the characteristics of a time-frequency hybrid waveform constructed by alternating OFDM and LFM time slots. The horizontal axis of Figure 4(a) represents time, ranging from 0 to 2.5 microseconds, and the vertical axis represents frequency, covering 0 to 800 MHz. The color depth represents signal energy intensity. This hybrid waveform transmits OFDM and LFM signals by alternating between different time slots. The implementation uses the odd or even nature of the slot numbers to distinguish waveform types. The time-frequency spectrum shows that some time slots exhibit a discrete subcarrier structure, corresponding to an OFDM signal, while others display continuous frequency modulation characteristics, consistent with LFM signals. The different fluctuation patterns of the real and imaginary components of the time-domain waveform also reflect the alternating appearance of these two waveforms. In Figure 4(b), the horizontal axis represents time from 0 to 100 microseconds, and the vertical axis represents signal amplitude. The maximum amplitude of the real part is approximately ± 10, and the imaginary and real parts vary alternately, indicating that the signal exhibits good complex waveform characteristics.

E. DUAL-OBJECTIVE OPTIMIZATION OF ADAPTIVE WEIGHTS

The proposed joint design algorithm employs a two-stage iterative optimization process: first, before the start of each OFDM frame, the current Doppler frequency shift f_d is obtained based on pilot estimation, and the Symbol-Level Precoding (SLP) matrix P_{SLP} is initialized accordingly. Then, with the P_{SLP} fixed, the M intra-pulse polyphase code sequence $\{\phi_m\}_{m=1}^{M}$ is solved to minimize the Doppler sidelobe energy. After the phase code converges, the detection probability P_d of the sensed target is re-evaluated. If its increase exceeds the threshold $\epsilon = 0.02$, the SLP weights are updated and the iteration continues. This joint optimization is performed for a maximum of three rounds to achieve a balance between computational overhead and performance gain. The entire process is executed in the baseband processing unit at the frame level (100 μs) to ensure the real-time requirements of the 6G system.

In 6G high-speed mobile environments, the performance of communication and perception systems is significantly affected by Doppler shift and the time-varying characteristics of the channel. Optimizing a single performance metric cannot meet these dual requirements. To achieve the coordinated maximization of communication rate and perception detection probability, this paper constructs an adaptive weight adjustment model based on multi-objective optimization theory. This model dynamically adjusts the weights of communication and perception performance using real-time Doppler estimation results, forming an optimal strategy that balances the two.

In the specific implementation, the target velocity variation range and channel time-varying rate are first quantified based on the Doppler shift estimate of the received signal, providing input parameters for the optimization model. The

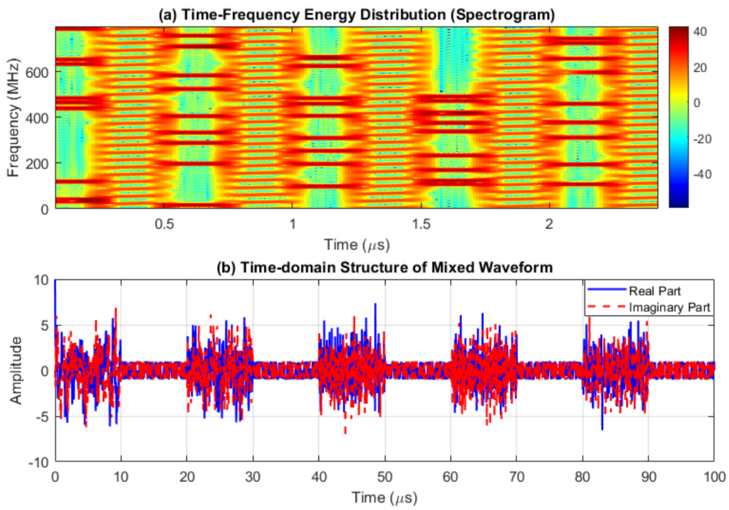

FIGURE 4. Time-frequency hybrid waveform construction (a) Time-frequency energy distribution (spectrum); (b) Time-domain structure of the hybrid waveform

communication performance metric is measured using a combination of instantaneous SNR and BER, while the perception performance metric uses target detection probability and false alarm rate (FAR) as evaluation criteria. The joint objective function is designed as the weighted sum of the communication rate R and the perception detection probability P_d, as shown in Formula 16:

$$J = \alpha(t) \cdot R + (1 - \alpha(t)) \cdot P_d \tag{16}$$

The weight factor $\alpha(t) \in [0, 1]$ is dynamically adjusted based on the real-time Doppler estimation to ensure that perception is prioritized in high-speed motion, and communication is prioritized in low-speed stable conditions. The weight adjustment strategy is implemented through a linear mapping function as shown in Formula 17:

$$\alpha(t) = 1 - \frac{f_d(t)}{f_{d,\max}} \tag{17}$$

$f_d(t)$ is the estimated value of the Doppler shift at the current moment, and $f_{d,\max}$ is the maximum estimated Doppler shift of the system. This mapping ensures that as the Doppler shift increases, the perception weight increases, and the communication weight decreases accordingly, achieving adaptive balance. To solve the above optimization objectives, this paper adopts an iterative algorithm based on gradient projection. First, the weight $\alpha(t)$ is initialized, and the corresponding communication rate and perception probability are calculated. Then, the gradient information is used to adjust the waveform parameters and resource allocation strategy to maximize the joint objective function. The algorithm process includes communication resource allocation adjustment, perception pulse design optimization, and Doppler compensation parameter update to ensure that the optimization path converges to the local optimal scheme. In terms of parameter setting, the communication rate calculation is based on the current channel capacity model and uses the Shannon formula as shown in Formula 18:

$$R = B \log_2(1 + \text{SNR}) \tag{18}$$

The perception detection probability is based on the statistical assumption of the target signal and noise and is evaluated using the Likelihood Ratio Test (LRT) in the classical detection theory.

In this scheme, the adaptive weight adjustment for dual-objective optimization is performed at the frame level, i.e., the weight factor α is updated every 100 μs (corresponding to one waveform frame). This timescale is jointly determined by the OFDM symbol period and the pulse repetition interval, which can track the maximum Doppler change rate of the target velocity at 150 m/s while avoiding the control signaling overhead caused by frequent symbol-level updates. Simulations show that at this timescale, the performance loss caused by the weight adjustment lag is less than 1.5%, effectively achieving a dynamic balance between communication and sensing.

III. PERFORMANCE VERIFICATION METRICS IN HIGH-SPEED SCENARIOS

To fully validate the performance of the proposed ISAC waveform co-design algorithm in 6G high-speed scenarios, experiments use a comprehensive simulation dataset modeled after a realistic high-speed mobile environment. This dataset covers a wide range of Doppler shifts, from zero rate to a maximum Doppler shift of approximately 5000 Hz, simulating typical 6G application scenarios such as high-speed vehicles, UAVs, and high-speed trains. The channel model uses a time-varying Rayleigh fading channel combined with additive white Gaussian noise to realistically reflect the time-varying channel characteristics and multipath effects caused by high-speed mobility. Target echo signals include a combination of multiple targets with varying ranges, velocities, and reflection cross-sections, ensuring a comprehensive evaluation of perception performance. The dataset also incorporates various interference environments, including background clutter and system noise, to verify the robustness of the algorithm. The sampling rate is set to 10 MHz, with a subcarrier spacing of 15 kHz, meeting the high-frequency bandwidth requirements of 6G. The data duration covers various mobility state transitions.

All experiments are conducted on the MATLAB R2024b platform, running on an Intel i9-13900K with 64GB of RAM. The simulation scenario is set to a maximum target velocity of 150 m/s (corresponding to a Doppler frequency shift of approximately 5 kHz and a carrier frequency of 30 GHz), with a time-varying Rayleigh fading model for the channel, a maximum Doppler spread of 5 kHz, and 6 paths. The baseline schemes include: (1) pure OFDM-ISAC (without Doppler compensation); (2) pure LFM radar + independent communication link; (3) OFDM waveform with only SLP compensation (without intra-pulse modulation). All schemes use the same bandwidth (800 MHz), sampling rate (10 MHz), and SNR range (-10~20 dB) to ensure fair comparison.

A. BIT ERROR RATE

BER is a core metric for measuring the transmission quality of a communication system, reflecting the proportion of error bits in the received data. The evaluation process first simulates a channel in a high-speed mobile scenario to generate a received signal with Doppler interference. Signal demodulation and decoding are then performed. The decoded result is then compared bit by bit with the original transmitted data, and the number of bit errors is counted. The BER is defined as the ratio of the number of errored bits to the total number of transmitted bits. By repeating the measurement under different SNRs, the system's BER curves under various environments are obtained, allowing the effectiveness of the waveform design in combating Doppler interference to be determined.

Figure 5 shows the bit error rate performance of various communication waveform schemes in multipath and Doppler environments. In Figure 5(a), the horizontal axis represents the signal-to-noise ratio (SNR, in dB), and the vertical axis represents the BER. It can be seen that as the SNR increases from 0dB to 20dB, the bit error rate of all schemes decreases significantly. Under static channel conditions (that is, no Doppler shift and no time-varying fading), the bit error rate is typically much lower than under moving targets or time-varying channels. The scheme proposed in this paper exhibits low bit error rates under all SNR conditions, and its overall noise immunity performance is superior to that of pure OFDM, pure LFM, and compensation-only schemes. In Figure 5(b), the horizontal axis represents target velocity (m/s), and the vertical axis represents BER. With a fixed SNR of 10 dB, the bit error rate generally increases as speed increases from 0 to 150 m/s. However, the proposed scheme experiences a smaller increase in bit error rate, while the pure OFDM and pure LFM schemes experience a significant increase in bit error rate, demonstrating that the proposed scheme is more robust in high-speed mobile environments.

B. PERCEIVED TARGET DETECTION PROBABILITY

The perceived target detection probability refers to the probability that the system successfully detects a real target. During testing, target echo signals in a high-speed dynamic scene are processed and detected based on the received noise. By setting different detection thresholds, the number of correctly identified targets in multiple trials is counted. The detection probability is calculated as the ratio of the number of correct detections to the number of target appearances. This metric reflects the system's sensitivity and reliability to targets under the influence of Doppler shift and clutter, and demonstrates the performance of the perception module under high-speed conditions.

Figure 6 illustrates the target detection probability of the ISAC system as it varies with SNR in a 6G environment. Figure 6(a) shows the SNR (dB) on the horizontal axis and the detection probability Pd on the vertical axis, reflecting the variation in detection performance at speeds of 0, 50, 100, and 150 m/s. The results show that as the SNR increases from -10 dB to 20 dB, the detection probability significantly increases. At higher speeds, the probability is lower than at lower speeds, demonstrating speed-related performance degradation. Figure 6(b) analyzes the detection performance of targets with different RCSs (Radar Cross Sections) at a fixed speed of 100 m/s. The horizontal axis shows SNR, and the vertical axis shows Pd. The results show that targets with larger RCSs can achieve a higher probability of detection at the same SNR. For example, at an RCS of 5 dBsm, the Pd is close to 0.5 at an SNR of 10 dB, while at an RCS of -10 dBsm, the Pd is only approximately 0.38 under the same conditions. These results demonstrate the significant impact of high mobility and target scattering characteristics on ISAC perception performance.

C. FALSE ALARM RATE

The false alarm rate indicates the frequency with which the system incorrectly determines the presence of a target and assesses the reliability of the perception system. During the evaluation process, multiple detection experiments are conducted under targetless or static background conditions, and the number of false triggers is recorded. The false alarm rate is calculated as the ratio of false alarms to the total number of detections. A lower false alarm rate indicates that the system is better able to distinguish real targets from noise interference in complex environments. This metric is important for ensuring stable system operation and reducing false alarms.

Table 1 shows the FAR performance of different waveform schemes under varying clutter intensities, evaluating the system's detection reliability in complex environments. The proposed scheme exhibits low false alarm rates at all

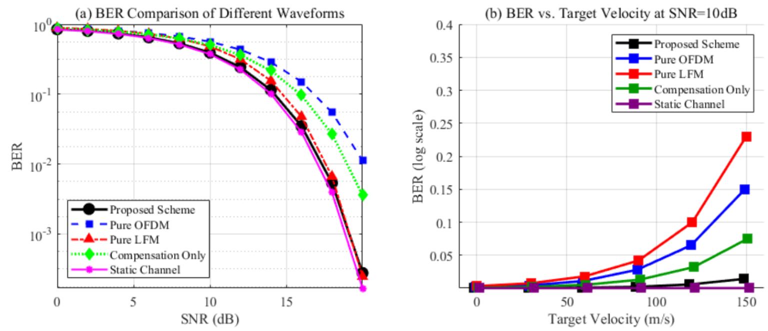

FIGURE 5. Comparison of communication system bit error rate performance (a) BER curves of various waveform schemes at different SNRs; (b) Comparison of bit error rates at different target velocities with a fixed SNR of 10dB

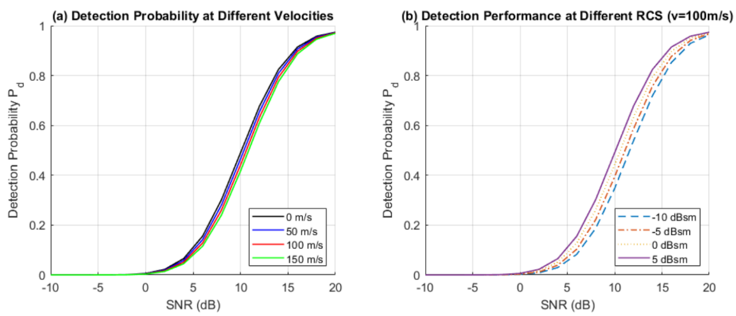

FIGURE 6. Comparison of target detection probability under different conditions (a) Detection probability variation with SNR at different speeds; (b) Detection probability variation with SNR at different RCSs

clutter intensities. For example, at a clutter intensity of 0 dB, the false alarm rate is only 8.2×10^{-5}, significantly lower than the 5.0×10^{-4} of pure OFDM and the 2.1×10^{-4} of pure LFM, demonstrating stronger clutter immunity. As the clutter intensity increases, the false alarm rate of the proposed scheme slowly rises to 9.5×10^{-4}, still significantly lower than the 1.2×10^{-2} of pure OFDM at 30 dB. The average false alarm rate of the proposed scheme is 3.73×10^{-4}, significantly better than the 43.75×10^{-4} of pure OFDM and the 30.4×10^{-4} of the compensation-only scheme, demonstrating the overall stability and reliability of the scheme. The false alarm rate is lowest under an ideal static channel, at 1.71×10^{-4}. This indicates that while the actual scheme cannot achieve ideal results, it has strong false alarm control capabilities and is suitable for application in complex dynamic environments.

D. RANGE RESOLUTION

Ranged resolution measures the system's ability to distinguish between closely spaced targets and is a key indicator of perception performance. This evaluation method quantifies the minimum distinguishable distance between two adjacent target echoes, based on the ambiguity function or pulse compression results of the echo signal. The test uses a simulated dual-target signal with a known distance interval, analyzing the peak separation of the echo waveforms in a high-speed moving environment. Higher range resolution indicates a system's ability to better resolve target distribution in complex scenarios.

Table 2 compares the performance of different waveform schemes in dual-target resolution and speed stability. Regarding resolution probability, when the target spacing is 0.2 meters, the proposed scheme achieves a resolution probability of 0.85, significantly higher than pure OFDM (0.20) and pure LFM (0.40). When the spacing increases to 1.0 meters, all schemes approach the ideal value ($\geq$0.95). Regarding range error, at a speed of 150 m/s, the proposed scheme produces only a 0.22-meter error, significantly lower than the 1.85-meter error of pure OFDM and superior to the 0.31-meter error of pure LFM. In particular, in stationary scenarios, the proposed scheme's 0.15-meter error approaches the ideal value of 0.10 meters, demonstrating its superior basic accuracy. The compensation scheme also underperforms the proposed scheme in both resolution probability (0.8) at a 0.5-meter spacing and error (0.58 meters) at 150 m/s, highlighting the necessity of a fusion design.

E. COMMUNICATION SYSTEM THROUGHPUT

Communication throughput is a measure of the system's actual data transmission rate. The evaluation is performed by sending a standard test data stream and measuring the amount of successfully received data after transmission over a high-speed channel. The test environment simulates the impact of the Doppler effect on the transmitted signal, and the net throughput is calculated by combining the bit error rate and re-transmission mechanism. Throughput reflects the system's bandwidth utilization efficiency and stability under dynamic, high-speed conditions and is an essential metric for measuring communication performance.

Figure 7 shows the communication throughput perfor-

TABLE 1. Comparison of FAR performance under different conditions

Waveform Scheme	Clutter Intensity = 0 dB	Clutter Intensity = 10 dB	Clutter Intensity = 20 dB	Clutter Intensity = 30 dB	Average FAR ($\times 10^{-4}$)
Proposed Scheme	8.2×10^{-5}	1.5×10^{-4}	3.1×10^{-4}	9.5×10^{-4}	3.73
Pure OFDM	5.0×10^{-4}	1.2×10^{-3}	3.8×10^{-3}	1.2×10^{-2}	43.75
Pure LFM	2.1×10^{-4}	5.5×10^{-4}	1.8×10^{-3}	1.2×10^{-2}	36.4
Compensation Only	3.5×10^{-4}	8.2×10^{-4}	2.5×10^{-3}	8.5×10^{-3}	30.4
Static Channel (Ideal)	2.0×10^{-5}	4.5×10^{-5}	1.2×10^{-4}	5.0×10^{-4}	1.71

TABLE 2. Range resolution performance comparison

Waveform Scheme	Resolution probability (0.2m)	Resolution probability (0.5m)	Resolution probability (1.0m)	Distance error (0m/s)	Distance error (100m/s)	Distance error (150m/s)
Proposed Scheme	0.85	0.98	1	0.15	0.18	0.22
Pure OFDM	0.2	0.65	0.95	0.8	1.25	1.85
Pure LFM	0.4	0.9	0.99	0.2	0.25	0.31
Compensation Only	0.55	0.8	0.97	0.3	0.42	0.58
Static Channel	0.95	1	1	0.1	0.1	0.1

mance of five waveform schemes under different signal-to-noise ratios and target velocities. In Figure 7(a), the horizontal axis is SNR (dB), and the vertical axis is throughput (Mbps). It can be seen that static channels maintain the highest throughput at all SNRs. Pure OFDM performs better at different SNRs. The proposed scheme outperforms pure LFM and compensation-only schemes at all SNRs, approaching 1200 Mbps in the mid-to-high SNR range (20 dB). In Figure 7(b), the horizontal axis represents the target velocity (m/s), and the vertical axis represents the throughput (Mbps). At a fixed SNR of 10 dB, the static channel throughput only decreases slightly, while pure OFDM experiences a significant decrease with increasing speed, dropping from 380 Mbps to 90 Mbps. The proposed scheme maintains a high throughput (200 Mbps) at high speeds (150 m/s), significantly outperforming both pure LFM and compensation-only schemes, demonstrating its superior fading and Doppler robustness in high-speed dynamic environments.

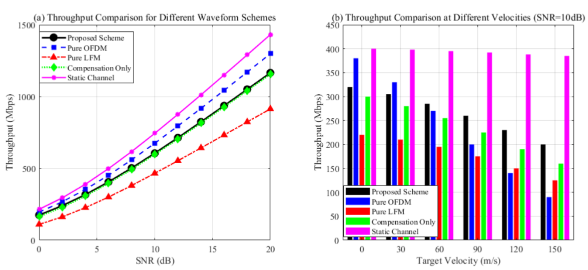

FIGURE 7. Communication throughput comparison (a) Throughput variation curves under different waveform schemes; (b) Throughput comparison bar chart at different speeds

IV. CONCLUSION

This paper addresses the issue of inefficient communication and perception fusion in 6G high-speed mobile environments by proposing a joint Integrated Sensing and Communication (ISAC) waveform design algorithm. Through Doppler sensitivity modeling, Doppler compensation pre-coding, intra-pulse modulation structure optimization, and time-frequency hybrid waveform construction, combined with dual-objective optimization of adaptive weights, a dynamic balance between communication rate and perception detection probability is achieved. Experiments demonstrate that the proposed method significantly improves communication reliability and perception accuracy in 6G high-speed mobile environments. At 150 m/s, the BER is only 0.22, lower than pure OFDM, and the false alarm rate is as low as 3.73×10^{-4}. The resolution probability for small targets as small as 0.2 m reaches 0.85, while the throughput remains at 200 Mbps. Despite these promising results, the proposed method's adaptability to extreme multipath and complex environments requires further enhancement, and the algorithm's computational complexity places high demands on real-time performance. Future work can focus on optimizing the algorithm's real-time computing capabilities and combining machine learning methods to enhance robustness in multi-target environments.

AUTHOR CONTRIBUTIONS

Xiaoyu Shen designed, collected and analyzed the data, and drafted the manuscript. Xiaoyu Shen conducted the study, critically revised the manuscript for important intellectual content, and gave final approval of the version to be published. Xiaoyu Shen participated fully in the work, take public responsibility for appropriate portions of the content, and agreed to be accountable for all aspects of the work in ensuring that questions related to the accuracy or integrity of any part of the work are appropriately investigated and resolved.

CONFLICTS OF INTEREST

The author declares no conflict of interest.

FUNDING

This research received no external funding.

ACKNOWLEDGEMENTS

Not applicable.

REFERENCES

[1] N. González-Prelcic, M. F. Keskin, O. Kaltiokallio, M. Valkam, D. Dardari, X. Shen, et al., "The integrated sensing and communication revolution for 6G: Vision, techniques, and applications," Proceedings of the IEEE, vol. 112, no. 7, pp. 676-723, 2024, doi: 10.1109/JPROC.2024.3397609.

[2] A. Kaushik, R. Singh, S. Dayarathna, R. Senanayake, M. D. Renzo, M. Dajer, et al., "Toward integrated sensing and communications for 6G: Key enabling technologies, standardization, and challenges," IEEE Communications Standards Magazine, vol. 8, no. 2, pp. 52-59, 2024, doi: 10.1109/MCOMSTD.0007.2300043.

[3] Z. Wei, H. Qu, Y. Wang, X. Yuan, H. Wu, Y. Du, et al., "Integrated sensing and communication signals toward 5G-A and 6G: A survey," IEEE Internet of Things Journal, vol. 10, no. 13, pp. 11068-11092, 2023, doi: 10.1109/JIOT.2023.3235618.

[4] F. Liu, Y. Cui, C. Masouros, J. Xu, T. X. Han, Y. C. Eldar, et al., "Integrated sensing and communications: Toward dual-functional wireless networks for 6G and beyond," IEEE Journal on Selected Areas in Communications, vol. 40, no. 6, pp. 1728-1767, 2022, doi: 10.1109/JSAC.2022.3156632.

[5] R. Singh, A. Kaushik, M. Dajer, and M. D. Renzo, "ISAC standardization and synergies with key technology enablers: overview and future prospects," Integrated Sensing and Communications for Future Wireless Networks, pp. 397-408, 2025, doi: 10.1016/B978-0-44-322143-9.00029-1.

[6] C. Zhao, H. Sun, T. Zhang, H. Luo, Y. Wang, Y. Jiang, et al., "Integrated Sensing and Communications Framework for 6G: Key Technologies and Hardware Prototype Validation," Journal of Electronics & Information Technology, vol. 47, no. 4, pp. 1-16, 2025, doi: 10.11999/JEIT241114.

[7] N. Chen, J. Zhao, F. He, N. Jiang, F. Zhang, and W. Jia, "Research on Integrated Sensing and Communication Technology of Unmanned Aerial Vehicles," Computer Simulation in Application, vol. 3, no. 1, pp. 53-56, 2025, doi: 10.18063/csa.v3i1.915.

[8] N. Chen, J. Zhao, W. Jia, F. He, H. Hu, and W. Jin, "A Review of Integrated Sensing and Communication of Unmanned Aerial Vehicle Swarms," Computer Simulation in Application, vol. 3, no. 1, pp. 18-22, 2025, doi: 10.18063/csa.v3i1.919.

[9] X. Wang, Z. Fei, Y. Zhou, and J. Hu, "Integrated sensing, communication, computation, and intelligence towards IoT: Key technologies and future directions," Journal of Electronics & Information Technology, vol. 47, no. 5, pp. 1-21, 2025, doi: 10.11999/JEIT240806.

[10] B. Clerckx, Y. Mao, Z. Yang, M. Chen, A. Alkhateeb, L. Liu, et al., "Multiple access techniques for intelligent and multifunctional 6G: Tutorial, survey, and outlook," Proceedings of the IEEE, vol. 112, no. 7, pp. 832-879, 2024, doi: 10.1109/JPROC.2024.3409428.

[11] R. Liu, M. Jian, D. Chen, X. Lin, Y. Cheng, W. Cheng, et al., "Integrated sensing and communication based outdoor multi-target detection, tracking, and localization in practical 5G networks," Intelligent and Converged Networks, vol. 4, no. 3, pp. 261-272, 2023, doi: 10.23919/ICN.2023.0021.

[12] C. Sun, L. Li, and H. Zhang, "OTFS-enabled integrated sensing and communication techniques for next-generation V2X networks," Chinese Journal of Engineering, vol. 45, no. 10, pp. 1674-1683, 2023, doi: 10.13374/j.issn2095-9389.2022.12.30.002.

[13] Z. Ma, Z. Li, and Y. Liang, "Overview and prospect of communication-sensing-computing integration for autonomous driving in the Internet of vehicles," Chinese Journal of Engineering, vol. 45, no. 1, pp. 137-149, 2023, doi: 10.13374/j.issn2095-9389.2022.04.16.003.

[14] D. Mohamed, A. Magdy, and A. Nasser, "Review of the Non-Orthogonal Multiple Access in 6G Technologies: Applications, challenges, and Future Directions," Suez Canal Engineering, Energy and Environmental Science, vol. 3, no. 3, pp. 42-59, 2025, doi: 10.21608/sceee.2025.379601.1077.

[15] A. Tang, F. Liu, W. Yuan, J. Yang, S. Wang, L. Lan, et al., "Signal Design for Communication Centric ISAC: State of Art and Future Aspects," Journal of Radars, vol. 14, no. 4, pp. 1019-1045, 2025, doi: 10.12000/JR25073.

[16] Y. Huang, J. Jin, M. Lou, J. Dong, D. Wu, L. Xia, et al., "6G mobile network requirements and technical feasibility study," China Communications, vol. 19, no. 6, pp. 123-136, 2022, doi: 10.23919/JCC.2022.06.010.

[17] Y. Liang, X. Yang, and F. Li, "An Extended Kalman Filtering Based Secure Transmission Scheme for Intelligent Reflecting Surfaces-assisted Integrated Sensing and Communication System," Journal of Electronics & Information Technology, vol. 47, no. 4, pp. 1052-1065, 2025, doi: 10.11999/JEIT240853.

[18] C. Zhen, J. Li, Z. Haijun, and Z. Wei, "Low-complexity channel estimation for RIS-assisted ISAC system," China Communications, vol. 22, no. 4, pp. 296-308, 2025, doi: 10.23919/JCC.fa.2024-0204.202504.

[19] R. Lo Cigno, F. Gringoli, S. Bartoletti, M. Cominelli, L. Ghiro, and S. Zanini, "Communication and Sensing: Wireless PHY-Layer Threats to Security and Privacy for IoT Systems and Possible Countermeasures," Information, vol. 16, no. 1, pp. 1-18, 2025, doi: 10.3390/info16010031.

[20] M. M. Adam, L. Zhao, K. Wang, and Z. Han, "Beyond 5G networks: Integration of communication, computing, caching, and control," China Communications, vol. 20, no. 7, pp. 137-174, 2023, doi: 10.23919/JCC.2023.00.039.